CHAPTER 4 ANISOTROPIC PLASTIC DEFORMATION

Advanced High Strength (AHS) steels have been increasingly applied in the automotive industries due to their distinguished mechanical properties. Microstructures of these steels play an important role and are designed by constituent phases with distinct characteristics. AHS steels exhibit sophisticated damage mechanisms, which make prediction of material formability difficult. In multiphase microstructures, early damage initiation is supposed, so that subsequent damage evolution strongly affects their plastic deformation behaviour. Obviously, the onset of damage becomes critical rather than strain localization, since the microstructure degradation introduced by the damage evolution could cause a qualitative alteration in material strength and ductility. The damage induced softening of material further governs plastic flow behaviour of such AHS steels after the damage initiation. Local distributed stress and strain in these steels could be distinctive. These unique characteristics led to the aim of this section, in which anisotropic plastic deformation of the AHS steels was studied.

This chapter describes the results presented in the published paper [67]. The influences of the constitutive models on plastic behavior of a TRIP steel were investigated. The von Mises's isotropic, Hill's anisotropic (Hill'48) and Barlat's anisotropic (Yld2000–2d) yield criteria were taken into account. The hardening laws with regard to the Swift and Voce model were examined. To determine material properties for different states of stress and loading directions, uniaxial tensile test, balanced biaxial test and disk compression test were performed. The yield stresses and *r*-values calculated according to each applied yield criterion were firstly compared with the experimental results. Afterwards, tensile test of sheet samples with various notch geometries as well as hole expansion test of the steel were carried out experimentally and simulated by FEM. The distributions of stress and strain within critical areas of each notched sample were determined and effects of the yield functions and hardening models on predicted stress triaxialities and plastic strain localizations were examined. In case of the hole expansion test, punch load–stroke curves, final hole diameters and strain distributions along the hole circumference and specimen diameter in the rolling and transverse direction were obtained and compared with the calculation results.

4.1 Introduction

In the automotive industries, vehicles designed under consideration of light weight, crash performance, energy saving and environmental aspect have been of special interest. Thickness reduction of steel sheet is desired due to lower fuel consumption and CO_2 emission. Passenger safety can be achieved using steels with increased ability for energy absorption. Thus, steel grades with higher strength and formability property are simultaneously needed. To meet these requirements Advanced High Strength Steel (AHSS) grades as Dual Phase (DP) steel, TRansformation Induced Plasticity (TRIP) steel, Complex (CP) steel have been continuously improved and employed [56]. The advantageous mechanical behaviors of the AHS steels are especially due to their complex microstructure morphologies and interactions between different phases. The microstructure of TRIP steels consists of retained austenite embedded in a primary matrix of ferrite and such stronger phases as martensite and bainite are present in varying amounts as well. Dispersion of hard second phases in soft ferrite causes high work hardening rate after yielding, as observed in the DP steels. In TRIP steels, the retained austenite can progressively transform to martensitic phase by increasing deformation. Therefore, decreasing rate of work hardening with plastic strain of these steels is much lower than the DP steels. This so-called TRIP effect phenomenon leads to a delay of necking that means higher formability of material [56,68]. Generally, a major challenge of these steels is to better understand their forming behavior. In recent years, there have been several contributions according to this issue [69-74]. For part making industries, these AHS steels are sophisticated materials, especially by designing forming process and corresponding tooling. More precise descriptions of flow behavior of such steels in sheet metal forming are still mandatory.

Formability behavior of the multiphase steels is controlled by apparent distinctions of mechanical properties of each microstructure constituent, in which different damage mechanisms can occur. In DP steels, for example, the ductile damage mechanism exhibited a rather complex situation. Voids were generated by debonding of phase boundaries, brittle cracking of the hard phase, as well as by inclusions and small precipitates. Consequently, possibilities of initiation of microcracks increased and subsequent damage evolution was thus strongly affected [64]. In TRIP steel, this void development resulted in an early damage initiation and continuous damage propagation impaired further local plastic deformation behavior of the material. Obviously, in such multiphase steels, onset of damage or damage initiation became critical rather than strain localization. The microstructure degradation introduced by the damage evolution could cause a significant change in material strength and ductility. Damage induced softening of materials continuously described flow behavior of material after the damage initiation. Some constitutive approaches incorporating damage occurrence have been currently reported for characterizing deformation and failure behavior of steels [64,75]. A proper description of the plastic deformation behavior is a strong requirement for a successful local failure criterion.

Numerous yield criteria have been proposed to represent anisotropic characteristic of sheet metals made of AHS steels and aluminium alloys [5-7, 76-79]. It has been shown that anisotropic coefficients and hardening laws have considerable effects on prediction of plastic deformation and formability [80-83]. Initially, Hill [6] incorporated material anisotropy by generalizing the von Mises criterion to give a quadratic yield function. Another family of yield functions was introduced by Bassani [76], in which relationship between the *r*-value (Lankford coefficient) and both uniaxial tensile and biaxial stresses were examined. Afterwards, the isotropic approach proposed by Hosford [77] was extended to a planar anisotropic model by Barlat et al. [78] using stress tensor invariants including term of shear stresses. Recently, the model have been further developed and often used to describe anisotropic characteristics of materials referred as Yld2000-2d yield criterion [7, 79]. Modelling of anisotropy behavior of AHS steels have been reported in [69-73]. Lee et al. [74] performed uniaxial tension, in-plane biaxial test for characterizing anisotropic properties of DP590 and TRIP590 steel sheets. Hereby, different yield functions and hardening models were evaluated. Among materials parameters obtaining by the uniaxial, in-plane biaxial and plane strain loading conditions, it was demonstrated that the anisotropic parameters of the Yld2000-2d yield criterion considering the biaxial state of stress provided better prediction of thickness strains than other criteria in biaxial stretch dominant region. For the TRIP590 steel, deviations between simulations and experiments were observed. This could be due to the strain induced martensitic transformation, which likely caused a change in the anisotropy and hardening behavior of the material. Lee et al. [84] also carried out the Limiting Dome Height (LDH) formability test and respective FE simulations. The results exhibited that for the Yld2000-2d model hardening curve and anisotropy values determined by the biaxial stress state led to significantly improved predictions. Formability of AHS steels in a deep drawing test was predicted using numerical FE simulations applying three yield functions, Hill’48, Barlat’89 and Banabic’2005 model by Wang et.al. [69]. It was concluded that hardening law according to Swift combined with Hockett-Sherby could well fitted the flow curves from uniaxial tensile test. The Barlat’89 yield model successfully predicted the onset of shear crack of the AHS steels. The deformation behavior of a dual phase steel sheet grade 780 subjected to hole expansion forming was investigated by Kuwabara et al. [85]. Experimental bi-axial tensile tests were performed for determination of anisotropic materials parameters. It was stated that the Yld2000-2d yield function with the *M*-exponent of 4 provided closer agreement with the experimental results than the von Mises and Hill’48 model. Toros et al. [86] studied both formability and springback characteristics of the TRIP800 steel using FE simulations. It was shown that the Yld2000-2d model calculated more accurate yield stresses and anisotropy values. The Yld2000-2d model also gave a better prediction of springback effect according to a V-die bending process. Chung et al. [72] experimentally and numerically examined hole expansion formability of steels TWIP940, TRIP 590 and 340R by simple tension tests. A damage model coupled with the Hill’48 yield criterion could well predict the hole expansion ratio (HER) of the steels. Obviously, the applied yield model influenced stress triaxialities and consequently prediction of material formability or onset of damage. Papaefthymiou et al. [87] found that increased stress triaxiality accelerated TRIP effect and damage development by promoting crack growth in the microstructure. Bao and Wierzbicki [66] used relationship between stress triaxiality and equivalent plastic strain as a criterion for predicting initiation of ductile fracture. Under high triaxiality condition void growth was the dominant failure mode, while at low stress triaxiality state fracture may develop as a combination of shear and void growth modes depending on the sample shape.

In this study, the anisotropic plastic behavior of the AHS steel grade TRIP780 was investigated. The TRIP steel exhibits a complex microstructure consisting of ferrite, bainite and small amounts of retained austenite. The austenite-martensite transformation, which took place during deformation, controlled high work hardening rate and formability of this steel. This material characteristic is very challenging for the automotive industries. Firstly, uniaxial tension, disk compression and hydraulic bulge test were carried out for the examined steels TRIP780. The normalized flow stresses, *r*-values and yield locus calculated according to three different yield criteria, the von Mises, Hill’48, and Yld2000-2d were verified with the experimental results. Subsequently, tensile tests of sheet samples with various notch shapes inducing different local stress triaxialities were performed. Stress and strain distributions in localized areas of the samples predicted by FE simulations were evaluated and discussed. In addition, stretch-flangeability of the steel was studied by hole expansion test with flat punch. Corresponding FE simulations of the hole expansion test were carried out using these yield functions. The numerical results were compared with the experimental ones in order to investigate influences of the yield criteria, hardening laws and material anisotropy on the description of plastic deformation under the stretch-flanging condition. The anisotropy behavior of this high strength steel under different states of stress was illustrated.

4.2 Anisotropic Materials Characterization

The AHS steel sheet of grade TRIP780 with an initial thickness of 1.2 mm was used in this investigation. The TRIP steel exhibited the microstructure containing ferritic matrix, bainite, retained austenite and small fraction of martensitic islands, as depicted in Figure. 4.1(b) When a TRIP steel is subjected to mechanical loads, phase transformation from the austenitic phase to the martensitic phase can occur [85, 86]. This formation of the harder martensite increases the rate of work hardening, which again raises the ductility of the steel. Thus, the TRIP steel can achieve higher total elongation than DP steel when comparing with the same grade or tensile strength [80]. Note that, in this work the TRIP effect was incorporated in the FE simulations by experimentally obtained flow curves. The transformation itself occurred in the formed samples was not modelled. Various mechanical tests were conducted for characterizing yield behaviors and stress-strain responses of the TRIP steel under different states of deformation, were expressed in Chapter 3.section 3.1

The phenomenological models according to the von Mises , Hill’48 and Yld2000-2d yield criteria were considered in this work for describing plastic anisotropic behavior of the investigated TRIP steel. The anisotropy could have significant influences on local material properties and thus forming behavior of the steel. In order to model the material anisotropy in a sheet metal, variation of yield stress and *r*-values with respect to the rolling direction must be first studied. A more definition overview of the applied yield models along with the methods for determining their corresponding anisotropic parameters were precisely discussed in Chapter 3 section 3.2.1 .

After obtaining all required materials parameters, flow stresses and *r*-values were numerically calculated by applying different yield criteria. The results were subsequently compared with the experimental ones in term of normalized flow stress and *r*-value depending on the angles to the rolling direction, as illustrated in Figure 4.1(a). It could be seen that the Yld2000-2d model provided well agreement for both flow stresses and *r*-values, while the von Mises model could not accurately represent the flow stresses and *r*-values in any directions, except the flow stress in the 0° direction. By the Yld2000-2d model, material properties in different directions were considered, but by the von Mises model single flow stress in the RD was used and *r*-value was not applied at all. However, it was noticed that the Hill’48 could fairly predict the *r*-value in all directions as the Yld2000-2d model, but its flow stress calculations were deteriorated in 45° and 90° direction, since the Hill’48 model just took into account the yield stress in the RD. Both yield stresses and *r*-values in the 45° and 90° direction of the investigated TRIP steel were higher than those in the 0° direction. The experimentally determined and numerically predicted yield locus or normalized TD stress as a function of normalized RD stress were presented in comparison in Figure 4.1(b). The Hill’48 yield model overestimated the experimentally obtained yield stress under uniaxial tension in the transverse direction (90°), but underestimated the yield stress under biaxial loading. The von Mises criterion underestimated the experimental yield stress in both states of stress. In contrast, the Yld2000-2d model precisely described the experimental yield stresses in every test directions.

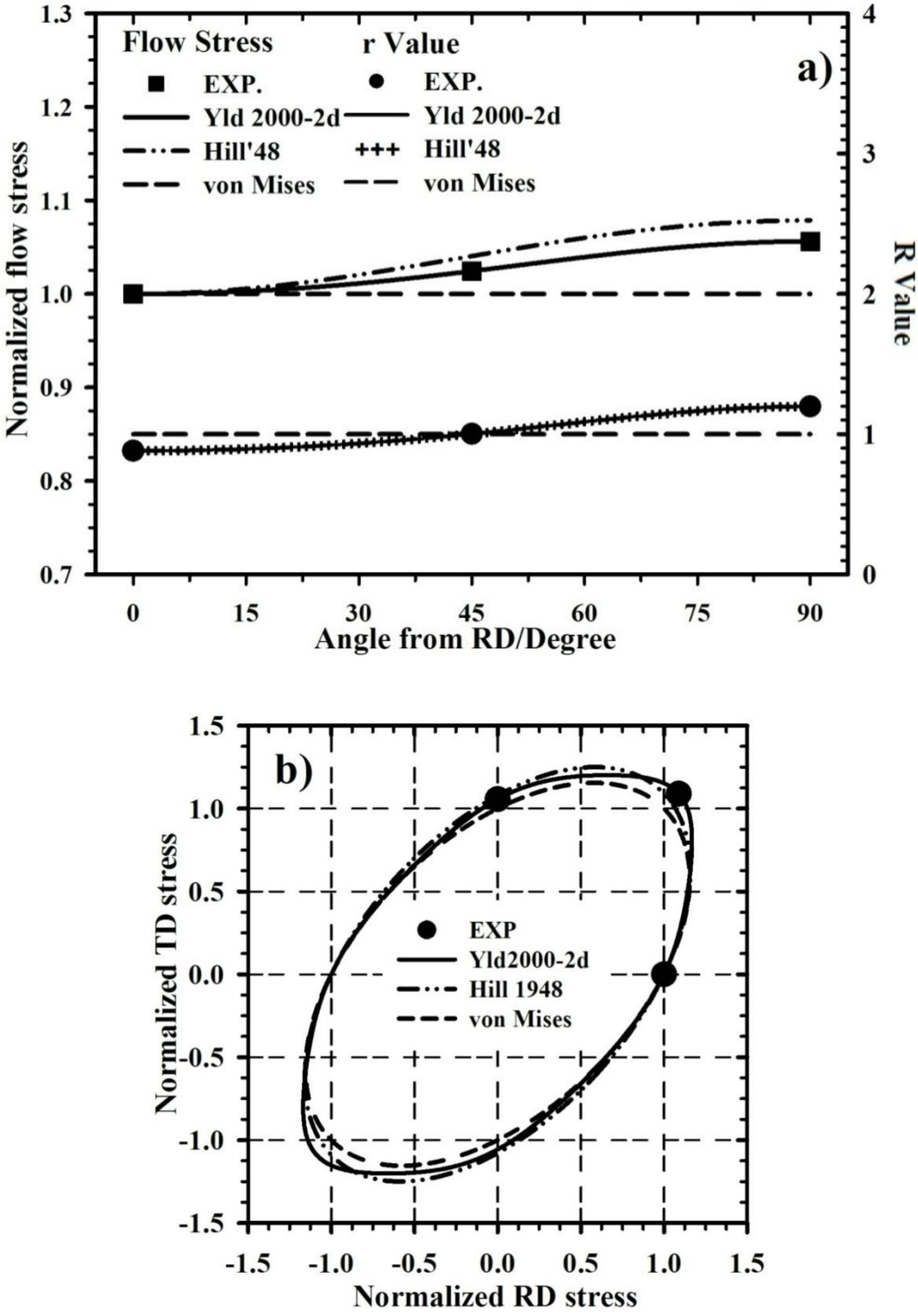

Figure 4.1 (a) Normalized flow stresses, *r*-values and (b) yield locus experimentally determined and numerically predicted by different yield criteria for the investigated steel in comparison

4.3 Application case studies

To verify influences of different constitutive hardening and yield models on the description of plastic deformation of the investigated high strength steel TRIP780, both tensile tests of various notched samples and hole expansion test were carried out. Experimental and numerical results were compared regarding local stress and strain distribution during forming.

4.3.1 Tensile test of notched samples

Tensile tests of sheet samples with various notch geometries were performed. Dimensions of the notched samples including V-shape, U-shape and radius-shape sample can be seen in Figure 4.2(a). These different notch shapes led to irregular local stress and strain development on the samples. All sample types were prepared in parallel to the rolling direction. Simultaneously, FE simulations of the tensile tests were carried out. By the FE modeling, 4-node shell elements with reduced integration (S4R) were used. Elastic-plastic material properties with rate-independent hardening with respect to the Voce and Swift law and the von Mises, Hill’48 and Yld2000-2d yield criterion were defined. Figure 4.2(a) shows the distribution of calculated effective stresses on the deformed samples at the moment of maximum loading states. Obviously, the various notches caused different local effective stresses and corresponding stress triaxialities on the samples during straining.

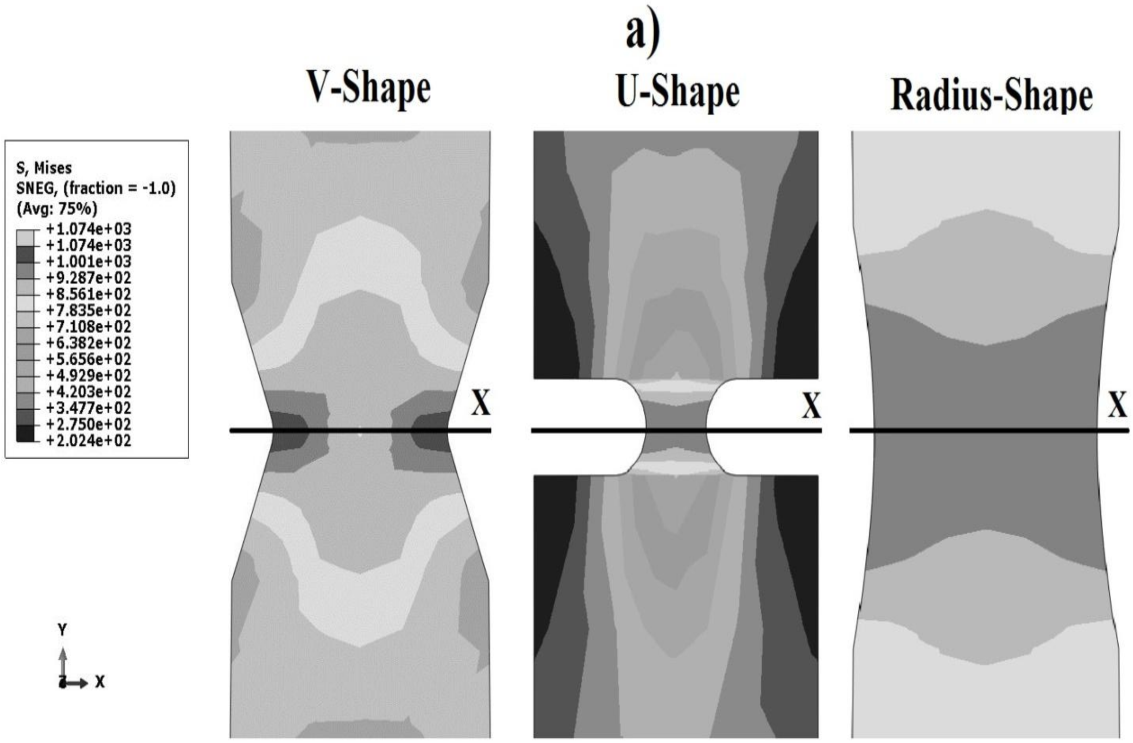

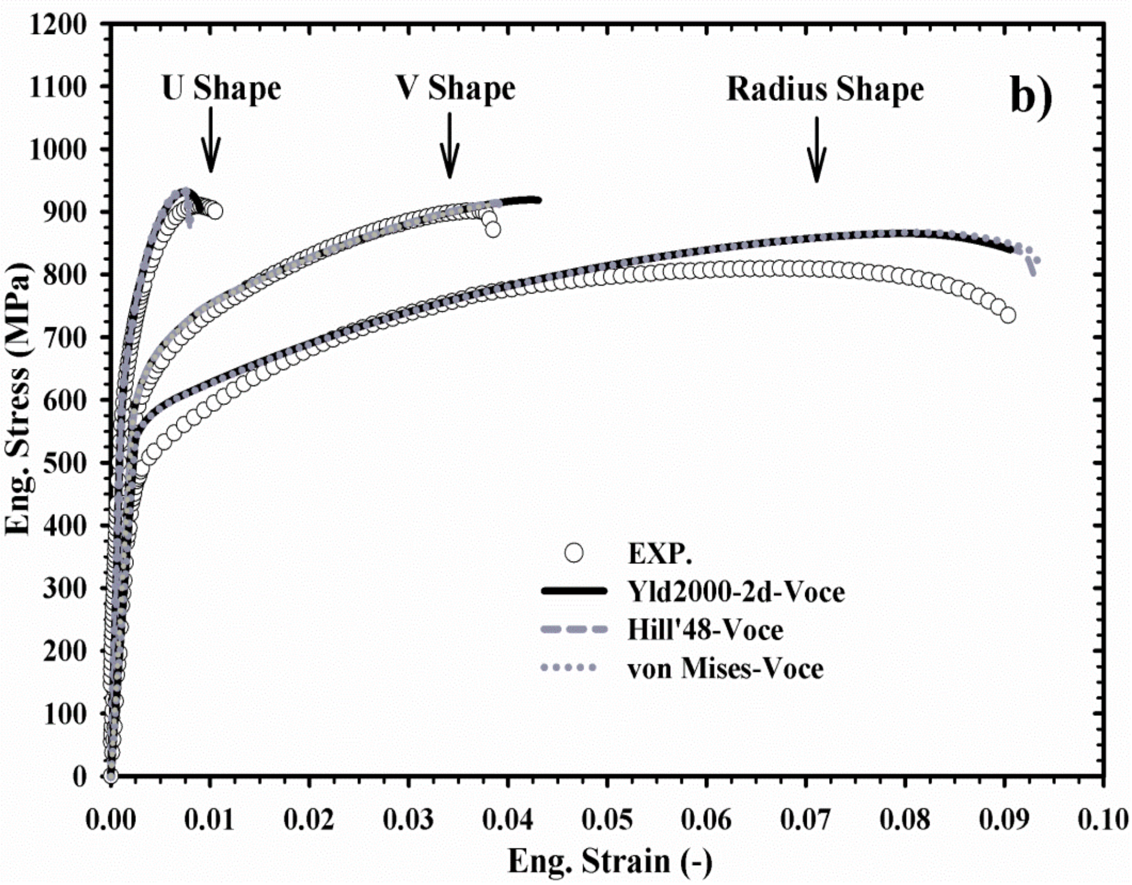

Figure 4.2 (a) Calculated effective stresses on the formed tensile samples with various notches at the moment of maximum loading states and (b) comparison of engineering stress-strain curves experimentally determined and numerically predicted by different yield criteria

From the tensile tests of various notched samples, experimentally determined stress-strain responses were compared with those calculated by the FE simulations and presented in Figure 4.2(b). The U-shape sample experienced highest stresses and failed at the earliest, since it had the most extreme cross section change. The V-shape and radius-shape samples sustained larger strains because of more homogeneously occurred plastic deformation. The engineering stress-strain curves predicted using all investigated yield criteria fairly agreed with the experimental results from low strain level up to an extent of strain before their maximum points. These overestimated curves before the maximum loads obtained from the simulations were due to an early damage initiation took place in the experiments. The damage onset and subsequent damage evolution in multiphase microstructure affected local plastic deformation and led to a prior softening of the high strength steel. These results were in accordance with a study by Lian et al. [64], in which onset of damage was detected before maximum force for various stress states. In addition, FE simulations were not coupled with any damage or failure criteria in this work. Therefore, calculated curves could not correctly describe effect of stress carrying capacity loss in the material and noticeable deviations between experimental and numerical stress-strain curves were observed after the maximum points.

4.3.1.1 Influences on stress-strain responses

Influences of different yield criteria and hardening models on stress-strain behavior of the investigated steel were illustrated by comparisons between numerically calculated and experimentally determined engineering stress-strain curves from the tensile tests. The results of V-shape, radius-shape and U-shape notched samples were shown in Figure 4.3(a)-Figure 4.3(c), respectively. It could be seen that stress-strain curves predicted by any yield criteria in combination with both Swift and Voce hardening laws were in well agreement with experimental curves up to the onset of damage. The stress-strain responses were not affected by the yield criterion, since isotropic hardening law was used. However, varying sample geometries caused somewhat different resulted stress-strain behaviors due to different stress states, as explained in details in and Lian et al. [64] and Bai and Wierzbicki [75].The stress-strain curves obtained by the Swift model were slightly higher than those by the Voce model. It could be noticed in Figure 3.10 that the Swift law provided somewhat higher flow curve than the Voce law at small strain values. From a plastic strain of around 0.25, the flow curve by the Swift model highly exceeded that by the Voce model. It was also observed that FE simulations applying the Swift model gave breaking points of the stress-strain responses at much higher strains than those from the Voce model for every notched sample. In comparison with the experimental results, the Voce model could better represent final failure states of the samples. In contrast, the Swift model predicted the experimental raptures more precisely than the Voce model in Figure 4.3(c), since the U-shape sample exhibited an extreme cross section change.

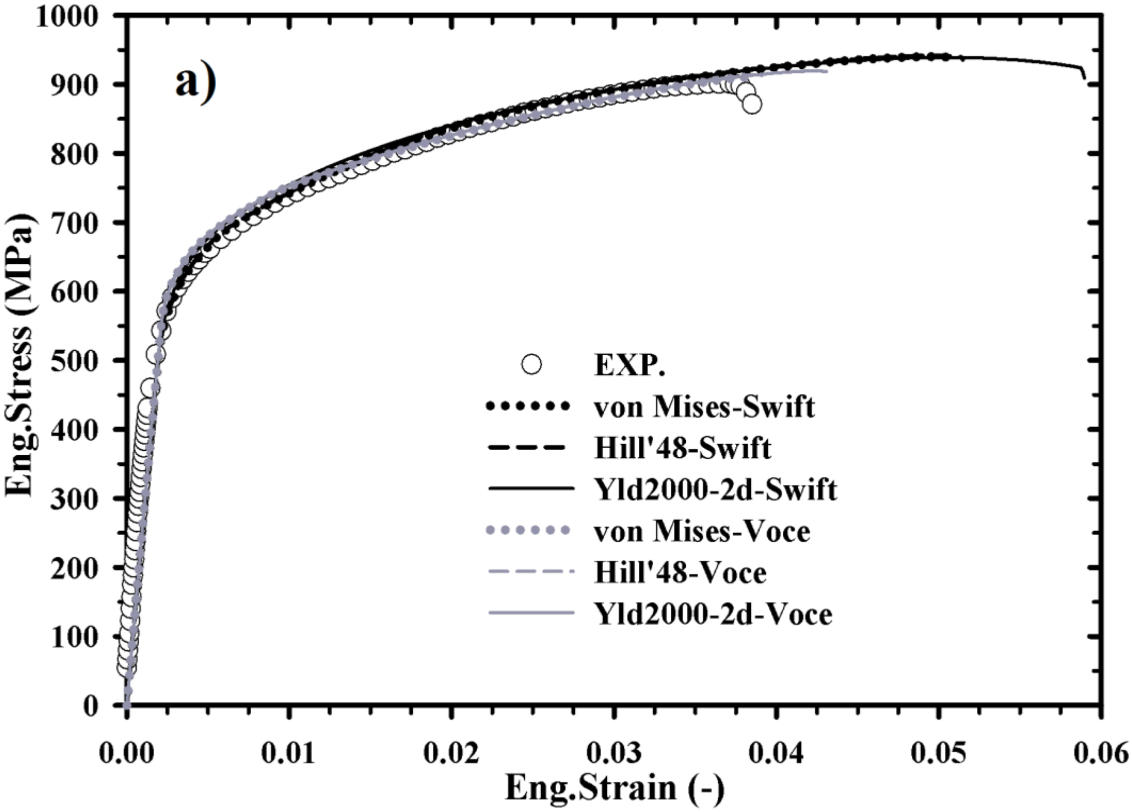

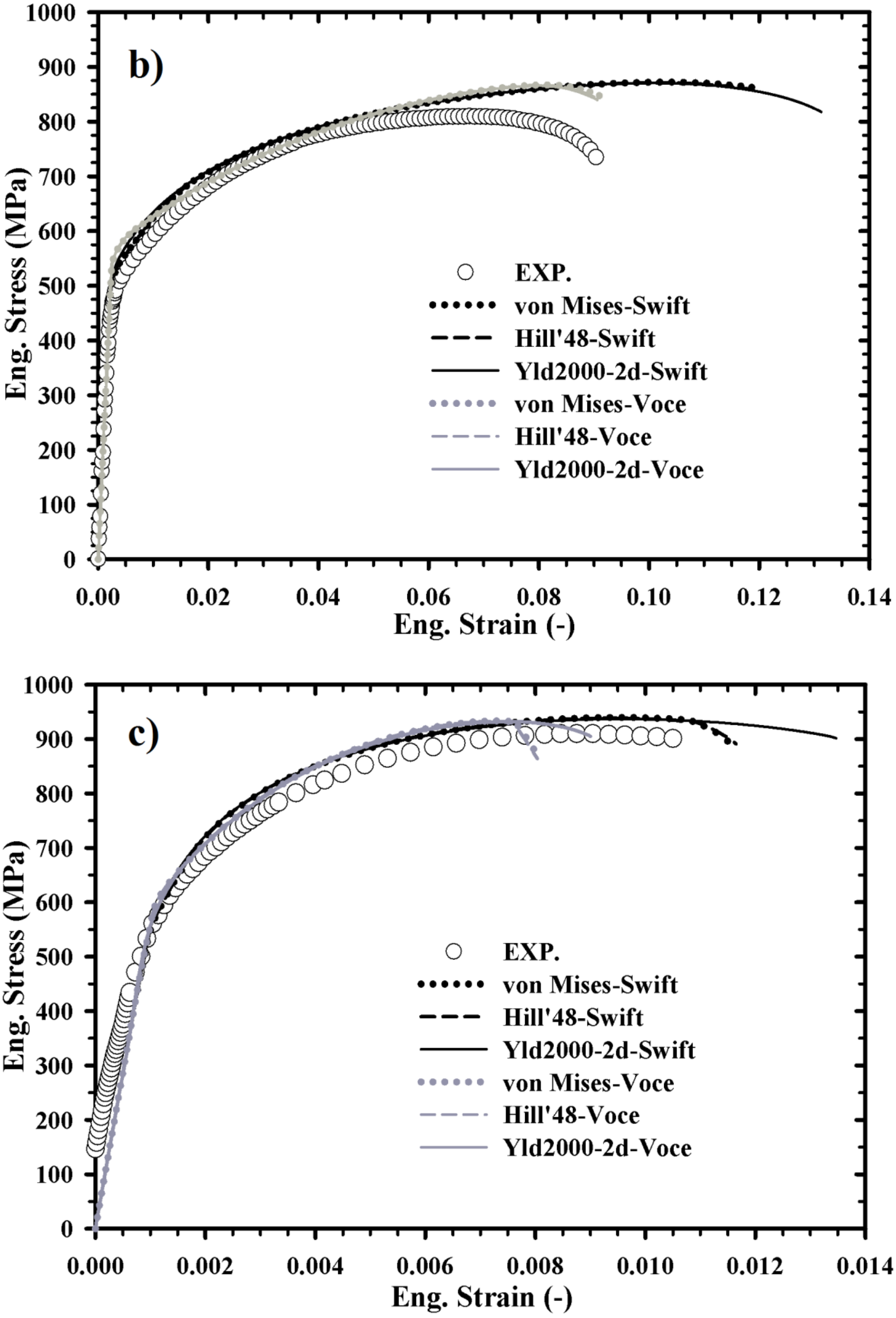

Figure 4.3 Comparison of engineering stress-strain curves experimentally determined and numerically predicted by different yield functions coupled with Swift and Voce hardening law for (a)V-shape sample (b)radius-shape sample and (c) U-shape sample

4.3.1.2 Influences on local stress-strain distribution

With regard to the used notch shapes, local stress triaxialities developed on each samples were varied during deformation. The stress triaxiality was defined as a stress ratio between hydrostatic pressure and equivalent stress. As aforementioned, onset of damage or damage initiation could considerably influence plastic deformation and damage induced material softening in experimental results of the various notched samples. Therefore, distributions of stress triaxialities along the x-axis, as depicted in Figure 4.2(a), in the middle of the samples with different notch shapes were calculated at the corresponding damage initiation states using different yield functions in combination with Voce type model and were demonstrated for instance in Figure 4.4(a). The equivalent plastic strains were also plotted in the same manner in Figure 4.4(b). Note that damage initiation was defined in this work when experimental and numerical stress-strain curves started to deviate from each other. Sample including sharp-edged notch like the V-shape sample exhibited higher stress triaxialities, whereas sample including smooth notch like the radius-shape sample significantly showed lower triaxiality values. The stress triaxiality values could be well correlated with ductile damage evolution in the steel, as reported in [64,53,66]. For such sample types, maximum stresses were observed in the middle area, while maximum equivalent plastic strains resulted at the border area. The V-shape sample showed the widest local triaxiality range among all notch samples.The range of equivalent plastic strains took place on the V-notch sample was largest as well. The plastic strains in the middle area of the sample with U-shape notch were higher than those of the samples with V-shape and radius-shape notch. The distributions of plastic strain on the V-shape sample were much inhomogeneous in contrast to those on the U-shape and radius-shape sample. A difference of plastic strain between middle and border area of up to 0.125 could be obtained. It was obvious that different yield functions provided both dissimilar local stress and strain distributions for all investigated states of stress. Thus, a prediction of subsequent failure onset could be definitely affected.

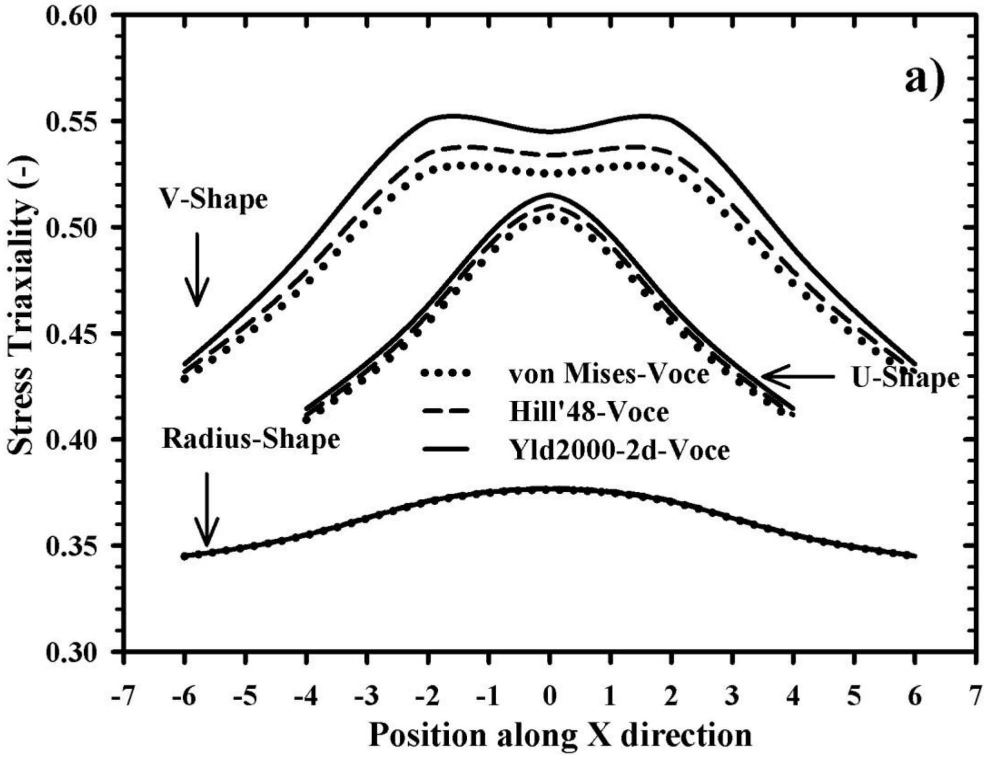

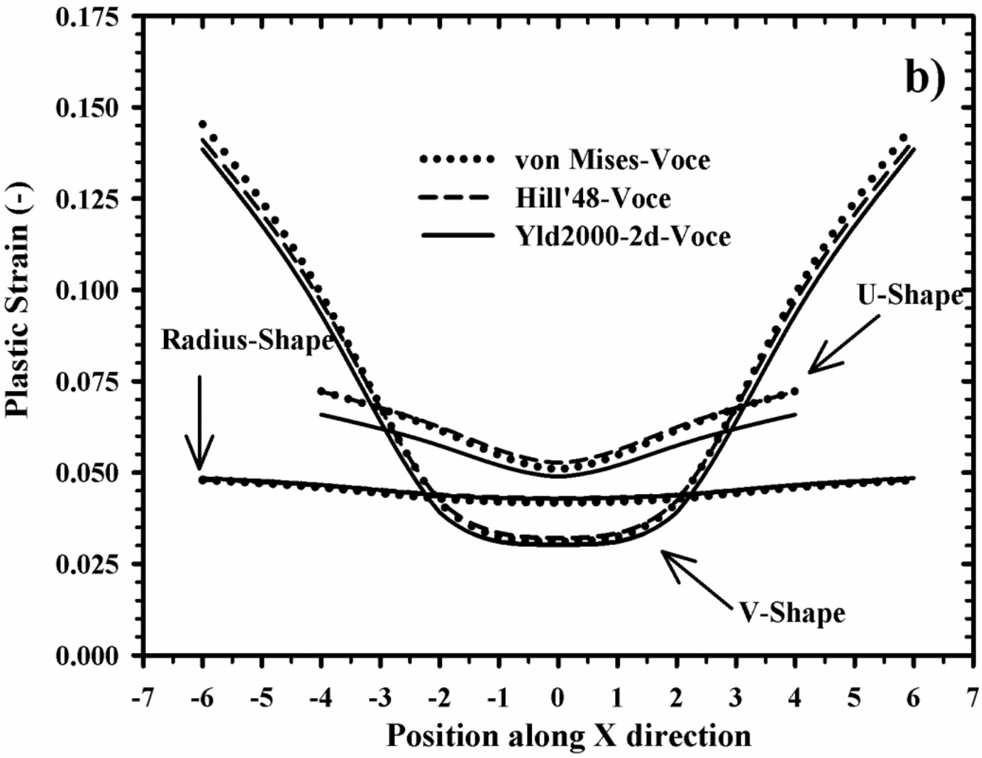

Figure 4.4 (a) Stress triaxialities and (b) equivalent plastic strains distributed along the *x*-axis in the middle of samples with different notch shapes calculated for the corresponding damage initiation states by different yield criteria.

Figure 4.5, 4.7 and 4.9 illustrated stress triaxialities along the x-axis in the middle of the V-, U- and radius-shape samples calculated by FE simulations applying different yield criteria and hardening models, respectively. With the same manner, equivalent plastic strains along the x-axis in the middle of the different samples were presented in comparison in Figure 4.6, 4.8 and 4.10. Hereby, influences of the used constitutive models and hardening laws on predicted local stress triaxiality and plastic strain were investigated with respect to the various states of stress. Significant effects of combinations of yield criteria and hardening models on both calculated stress triaxialities and equivalent plastic strains were found. Deviations of plastic strain and stress triaxialities up to a value of 0.08 and 0.03 were noticed, respectively. Particularly, in case of the V-shape sample representing a sharp-edged notch showed stronger effects of yield criterion and hardening model on the stress distributions than the other sample types. Apparently, higher stress triaxialities were obtained by the Yld2000-2d criterion in all sample shapes, with the exception of the radius-shape sample, by which variation of the stress triaxiality was little. The lowest stresses in all specimen types tended to be predicted by the conventional von Mises criterion. High stress triaxialities referred to high potential for TRIP effect and earlier crack initiation, since damage evolution mainly depends on the hydrostatic stress [66,86]. In contrast, with the exception of the radius- shape sample, equivalent plastic strains were slightly higher everywhere when calculated using the von Mises or Hill’48 yield function depending on the sample geometries and became lowest by the Yld2000-2d model. Note that all yield functions provided similar stress and strain gradients along the sample width for all notch shapes, but with different magnitudes. The gradients became more varying, when sharp-edged notch was taken into account.

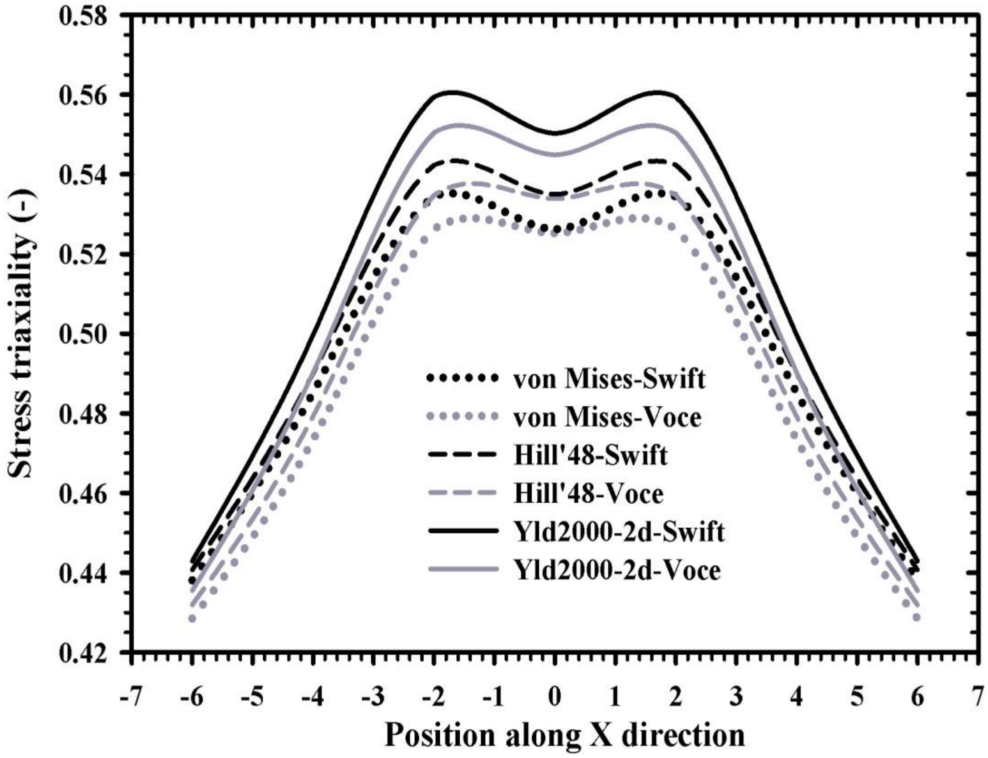

Figure 4.5 Stress triaxialities along the *x*-axis in the middle of V-shape sample predicted for the corresponding damage initiation states by different yield criteria and hardening

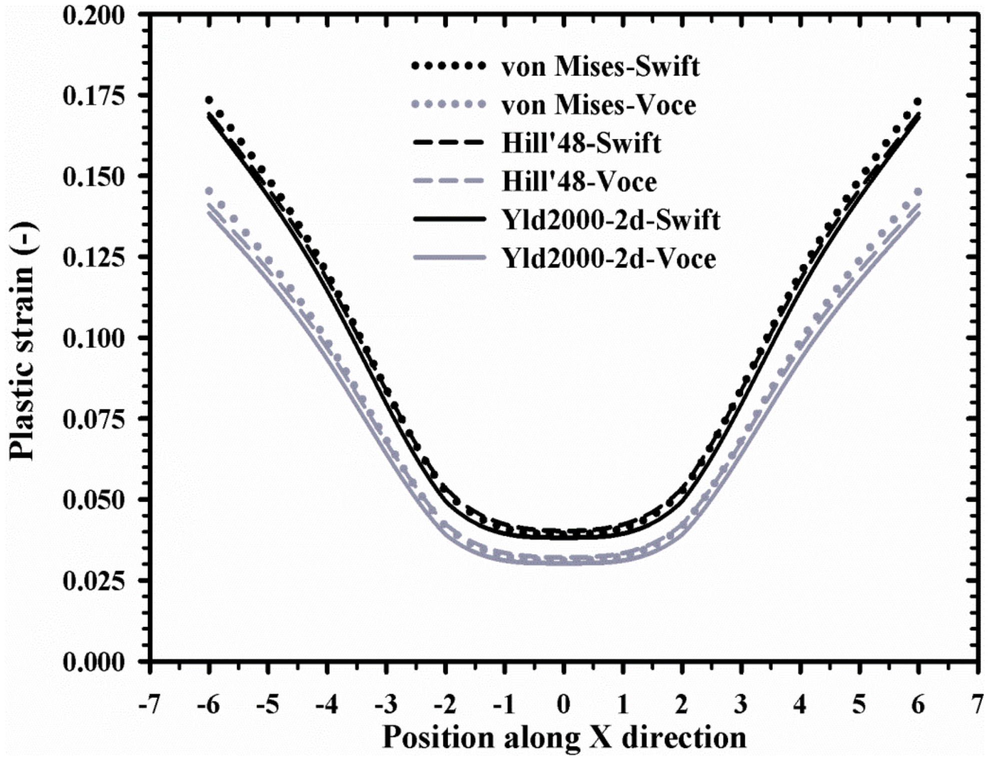

Figure 4.6 Equivalent plastic strains along the *x*-axis in the middle of V-shape sample predicted for the corresponding damage initiation states by different yield criteria and hardening laws.

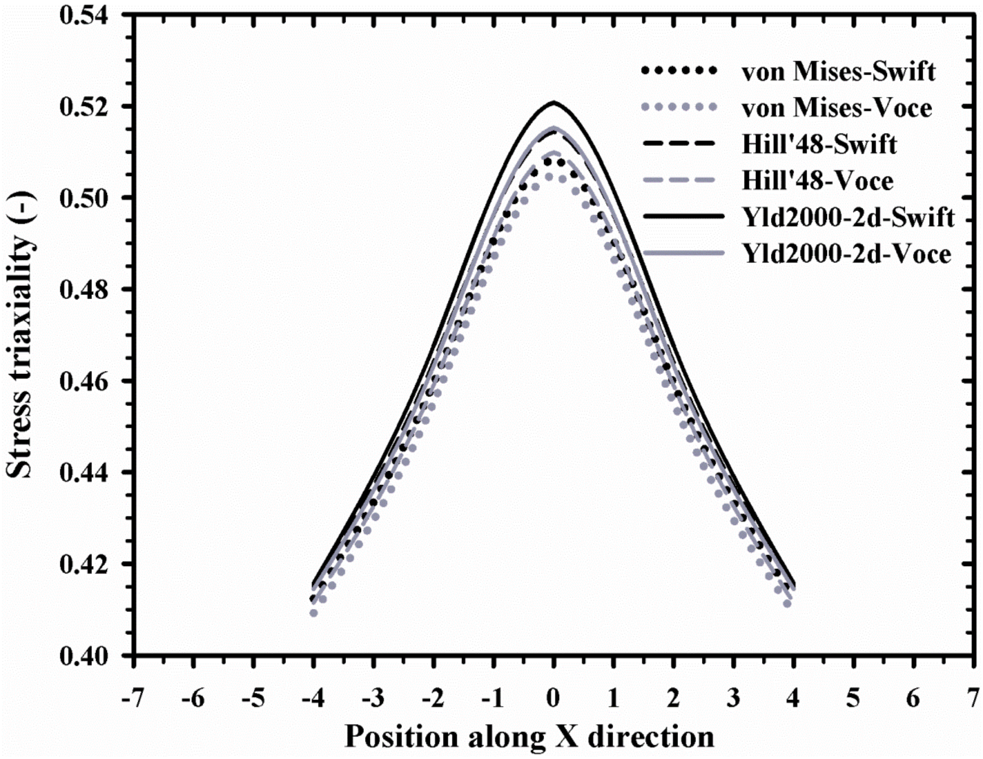

Figure 4.7 Stress triaxialities along the *x*-axis in the middle of U-shape sample predicted for the corresponding damage initiation states by different yield criteria and hardening laws.

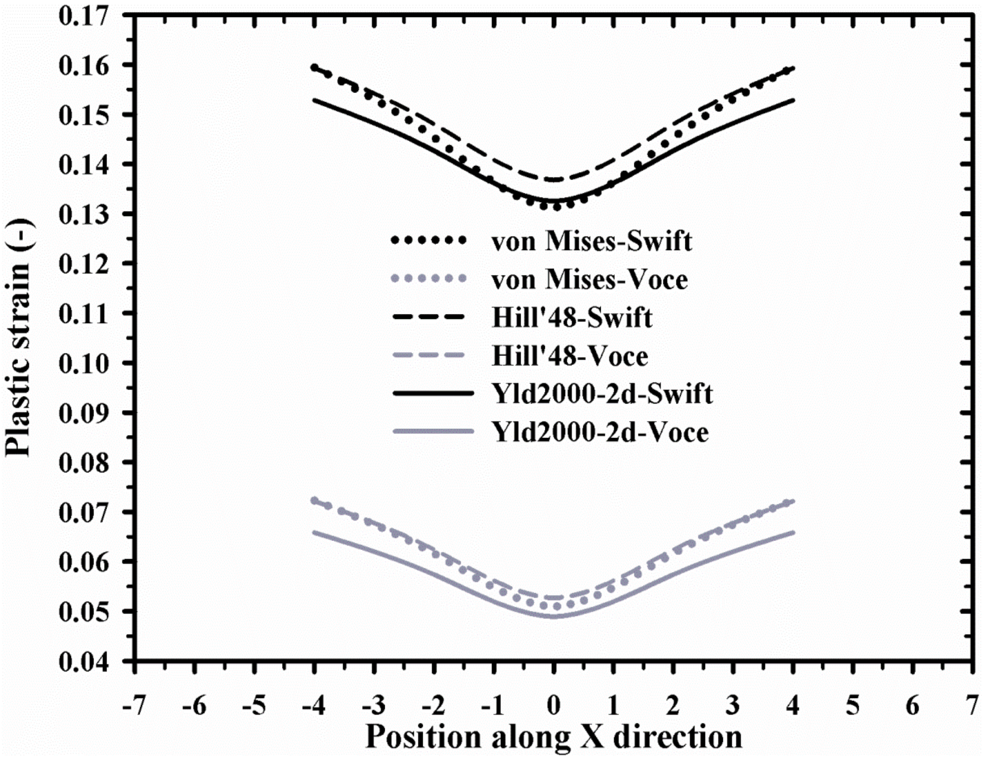

Figure 4.8 Equivalent plastic strains along the *x*-axis in the middle of U-shape sample predicted for the corresponding damage initiation states by different yield criteria and hardening laws.

Considerable effects of the hardening law could be also found from the results. Generally, the Swift model provided higher stress triaxialities than those given by the Voce model whatever which yield criterion was applied. Additionally, local plastic strains predicted by the Swift model were much higher than those calculated by the Voce model for all investigated yield criteria, especially in case of the U-shape sample. In the middle of the samples the deviations of stress triaxialities were higher and became smaller until the borders of the sample. In the vicinity of notch edges, maximum equivalent plastic strains occurred. The maximum local plastic strains ranged between 0.050 and 0.150 and were still lower than the overall maximum tensile strain of the investigated steel, as presented in Figure 3.10. The Voce model described a strain hardening rate, which was lower than the Swift model and eventually reached a saturated value. Thus, higher stress triaxialities in all sample types, especially in the middle of the samples, were predicted by the Swift law than by the Voce law. The plastic strains developed in all samples were lower than 0.25, beyond which flow stresses extrapolated using both hardening laws showed noticeable deviation. In other words, if occurred local plastic strains became then larger than this value, effects of the hardening law on stress distribution would be more pronounced. It could be concluded that with any types of yield criterion, stress triaxialities obtained from the Swift model were higher than those from the Voce model for every states of stress. Thus, the Swift type model provided also higher plastic strains than the Voce type model. This effect was especially increased in case of the samples with U-shape notch.

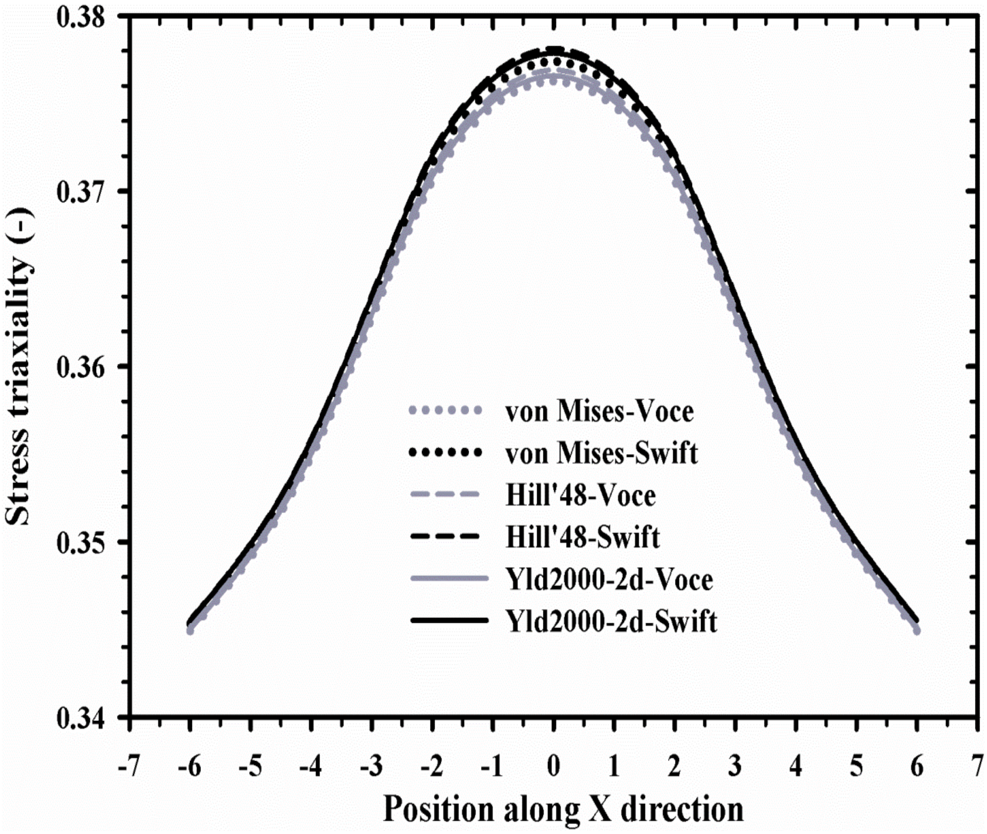

Figure 4.9 Stress triaxialities along the *x*-axis in the middle of radius-shape sample predicted for the corresponding damage initiation states by different yield criteria and hardening laws.

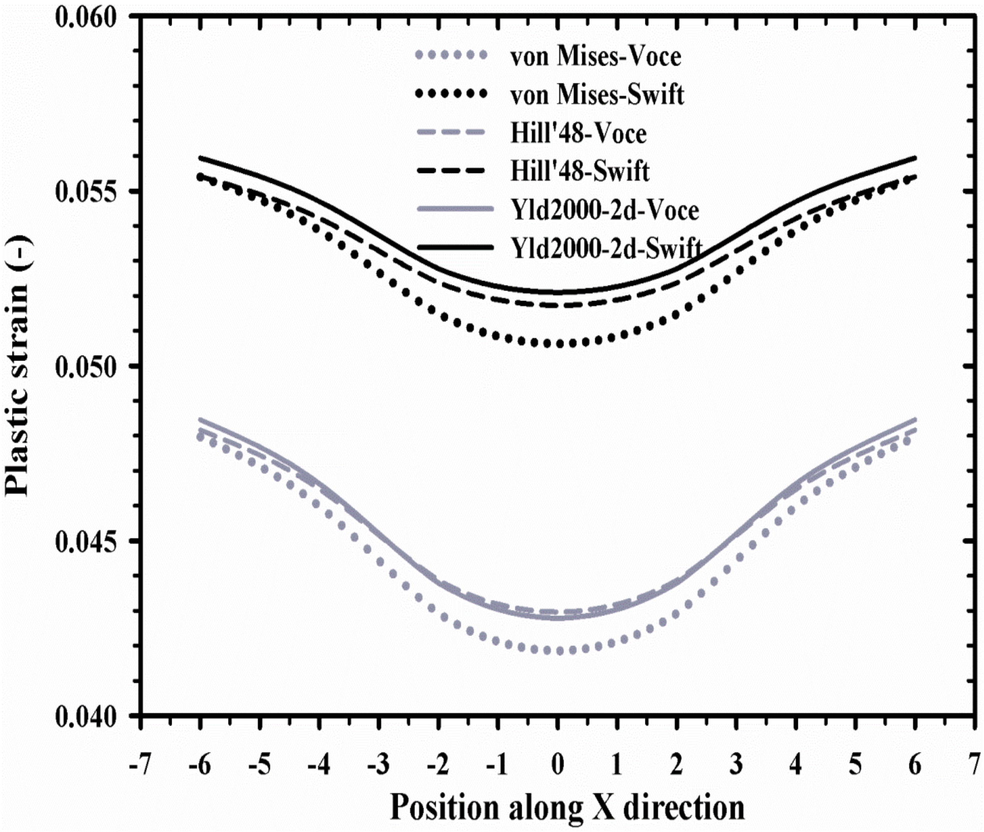

Figure 4.10 Equivalent plastic strains along the *x*-axis in the middle of radius-shape sample predicted for the corresponding damage initiation states by different yield criteria and hardening laws.

4.3.2 Hole expansion test

Hole expansion tests with flat bottom punch were performed on a universal sheet testing machine. Schematic view of the experiment was depicted in Figure 4.11. During the test, specimen with a central hole was firstly clamped between the blank holder and upper die. Movement of the outer sample periphery was prevented by means of a high constant blank holder force of 60 kN. Then, punch force was applied with a velocity of 20 mm/min. Once, the punch force suddenly dropped due to an appearance of crack, the test was terminated. The initial hole diameter d_0 was 12 mm. After the test, diameter of the enlarged hole, *d*, was measured. Punch load and stroke, thickness strain distribution on the specimen surface along the hole circumference and along the specimen diameter in the rolling and transverse direction were determined. For FE modeling of the hole expansion test, only one quarter of sheet specimen was defined due to the orthotropic material and full symmetry of the process itself. 4-node shell elements with reduced integration (S4R) and 5 integration points in the thickness direction were used for the sample FE model and is illustrated in Figure 4.12. A blank holder force of 60 kN as same as in the experiment was given. Between sheet and dies, a coulomb friction coefficient of 0.10 was defined. The punch, die and blank holder were modelled as analytical rigid surfaces and the steel sheet as elastic-plastic material. The yield functions, von Mises, Hill’48 and Yld2000-2d and the biaxial stress-strain curves extrapolated with the isotropic rate-independent hardening laws according to Voce and Swift were applied. The stress-strain responses of the TRIP780 steel obtained from the hydraulic bulge test were considered for both hardening laws, as shown in Figure 3.10.

Obviously, as shown in Figure 4.13, the 3D FE simulation model was combined with swift hardening law by using Yld2000-2d criterion, completely display.

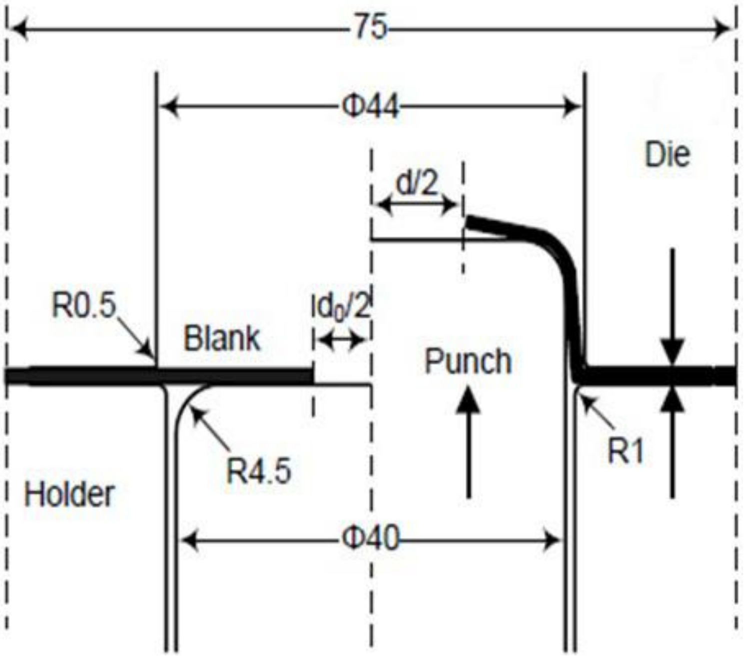

Figure 4.11 Schematic of hole expansion test using flat bottom punch (dimension in mm)

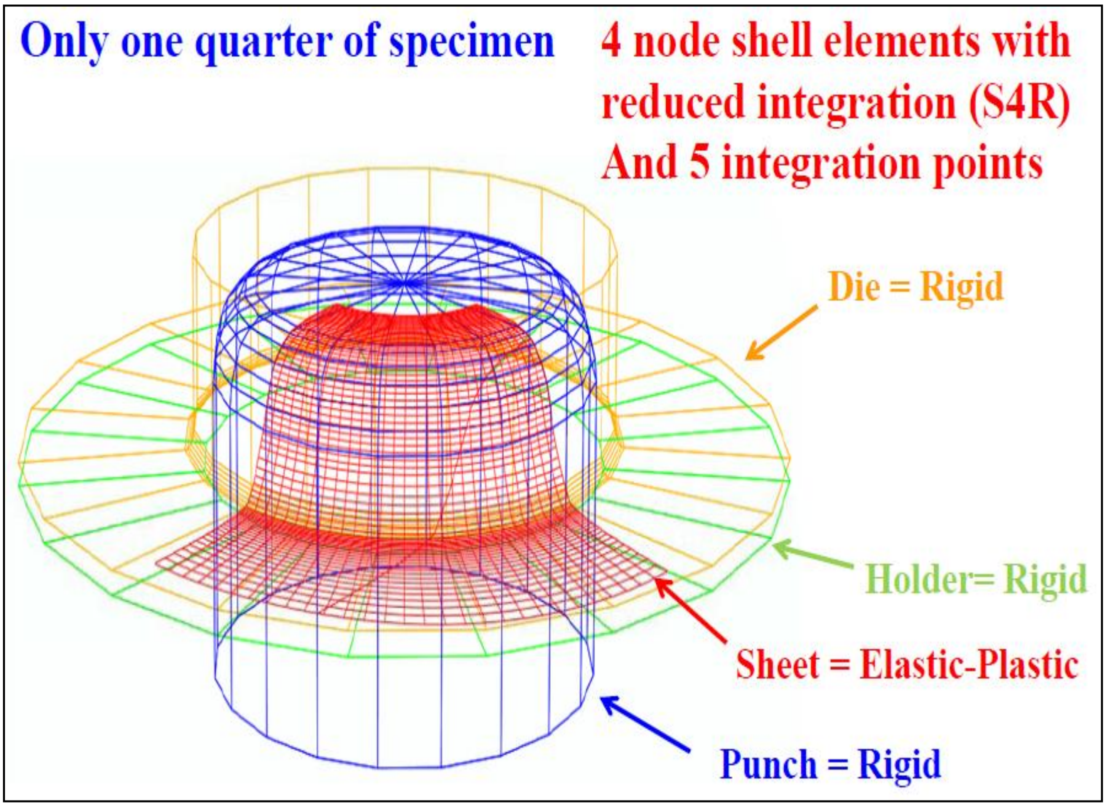

Figure 4.12 Schematic of finite element model for hole expansion test

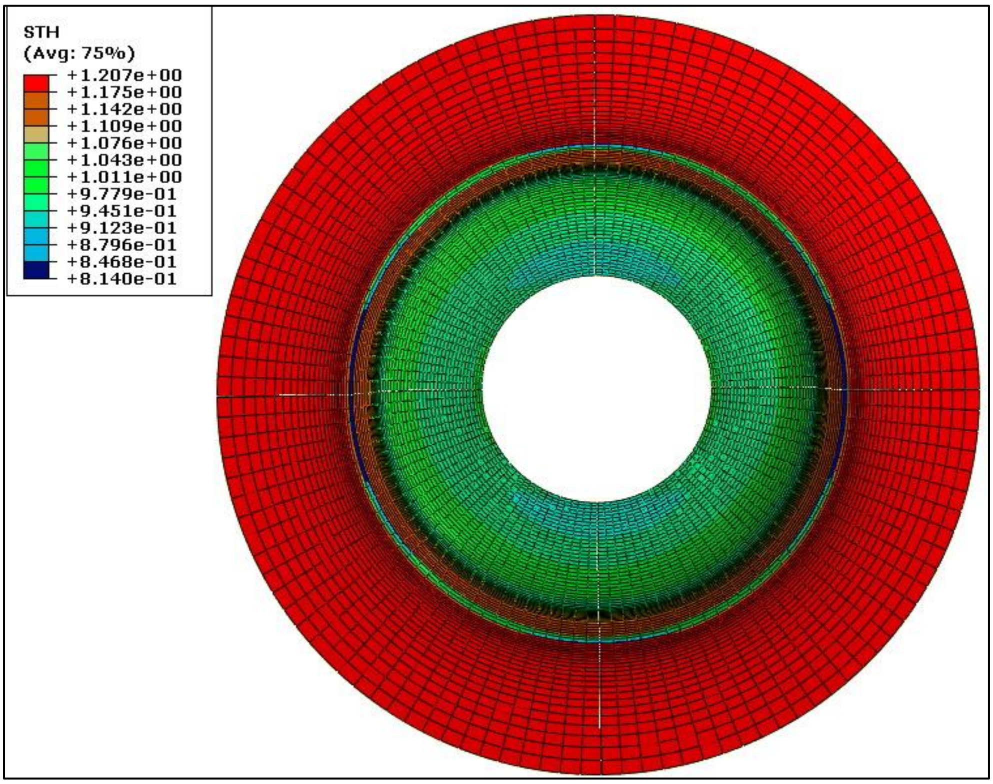

Figure 4.13 Sheet thickness distribution of 3D FE simulation model with Yld2000-2d

4.3.2.1 Influence on punch force and punch stroke

The punch forces and punch strokes experimentally measured and calculated by the FE simulations were compared in Figure 4.14(a) and Figure.4.14(b) for different combinations of yield criteria and hardening laws. Slightly influences of the yield criteria on the force-stroke curves could be observed. In Figure 4.14(a), it was found that the Yld2000-2d model with the *M* exponent 6 could more precisely predict the experimental curve when comparing with other yield criteria. The Hill'48 model overestimated and the von Mises model underestimated the experimental results, especially at higher punch strokes. According to effect of the hardening law, all simulations coupled with Swift law always provided higher force-stroke curves than those coupled with Voce law. This was due to that the Voce model exhibited much lower strain hardening rate beyond strain of 0.3 than the Swift model, as seen in Figure 3.10. Fig. 4.14(b) showed that force-stroke curve predicted by the Yld2000-2d yield criterion in combination with the Swift law was better in accordance with the experimental curve for both *M* exponents (6 and 7). It was noticed that simulation applying the *M* exponent 7 a bit underestimated the results from that using the *M* exponent 6 for all cases. With regard to the calculation of force-stroke curve influences of the *M* exponent could be neglected.

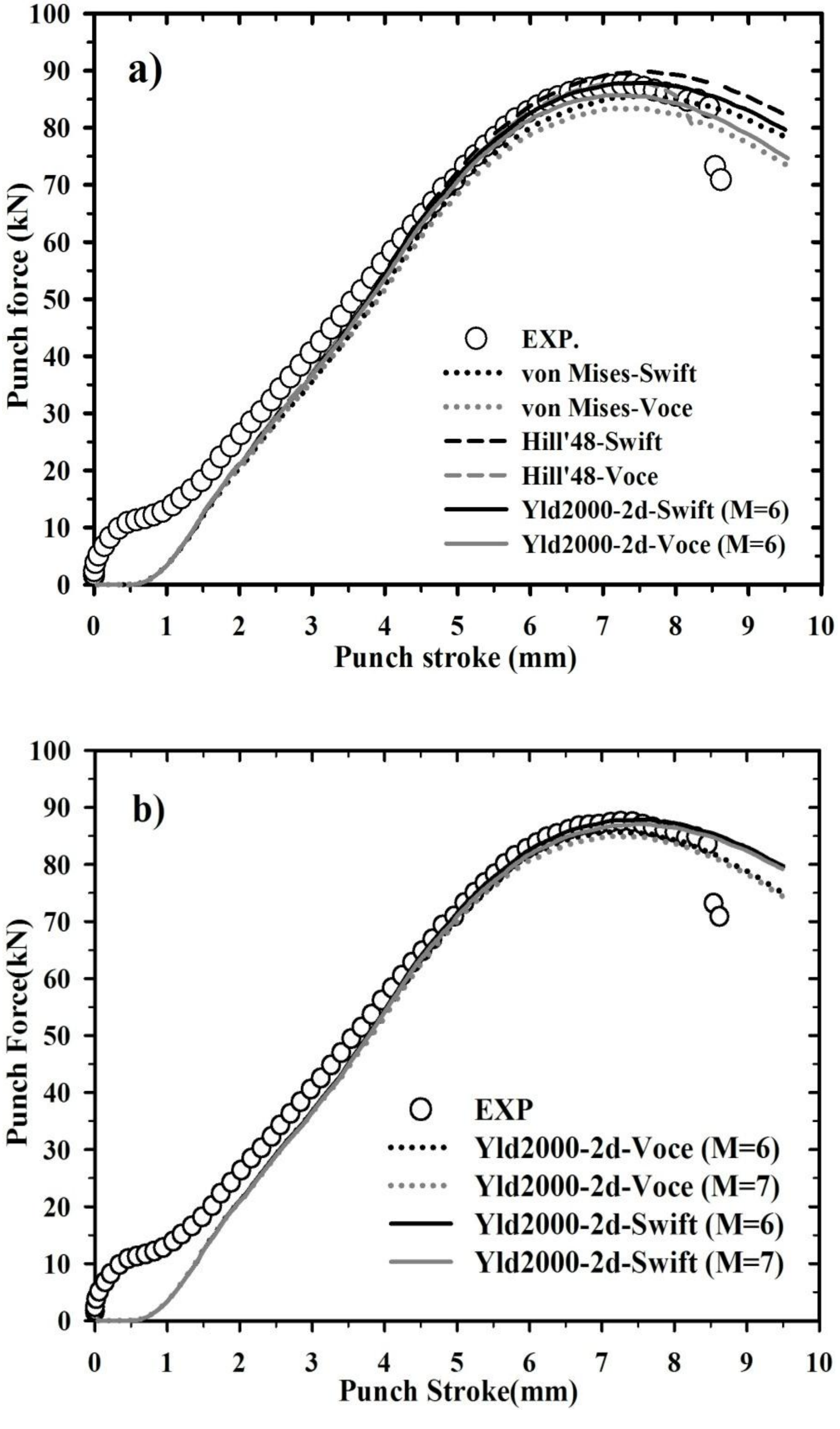

Figure 4.14 Comparison of numerically determined punch force-punch stroke curves using various yield functions in combination with different hardening laws with experimental results.

4.3.2.2 Influence on hole expansion ratio

Figure 4.15 shows the hole radii along the hole circumference at different angles in term of the hole expansion ratio, which were experimentally and numerically determined after failure at a punch stroke of about 8.5 mm, in comparison. The hole expansion ratio is generally utilised to specify formability of blank in a hole flanging process. It was calculated as a ratio between the initial hole diameter and the hole diameter at failure. As depicted in Figure 4.15(a), the von Mises and Hill’48 model predicted much lower hole expansion ratio than the experimental results. Nevertheless, the Hill’48 criterion gave correct tendency of the hole expansion ratio along the hole circumference, because the model also took into account the material anisotropy. Obviously, the Yld2000-2d model could fairly describe plastic deformation of the samples in hole expansion test in every direction. In case of the Yld2000-2d model, simulation using Swift hardening law provided more precise hole expansion ratio than that using Voce law. In general, the Voce model exhibited slightly higher hole expanding than the Swift model. In Figure 4.15(b) it was well illustrated that results from the Yld2000-2d model applying the *M* exponent 6 better agreed with the experiments than other combinations. The *M* exponent 7 led to lower hole expansion ratio than the *M* exponent 6 in every directions. All hole radii predicted by the *M* exponent 7 underestimated the experimental results. Note that different hole expansion ratio and hole radii measured along the hole circumference were directly affected by plastic anisotropy of the material. Regarding hole expansion of the investigated steel, the maximum hole radius of formed samples was observed at the RD and the minimum hole radius was at the TD. This anisotropic deformation could be well correlated with the *r*-value of the steel, in which the *r*-value from the RD was less than 1 and *r*-value from the TD was higher than 1, as given in Table 3.2. Therefore, during hole expanding material in the TD preferably deformed in the width direction rather than in the thickness direction and this led to a constraint of hole radius increase. For the investigated steel, crack formation occurred at the hole edge in the vicinity of the RD area that was in accordance with the maximum hole radius observed.

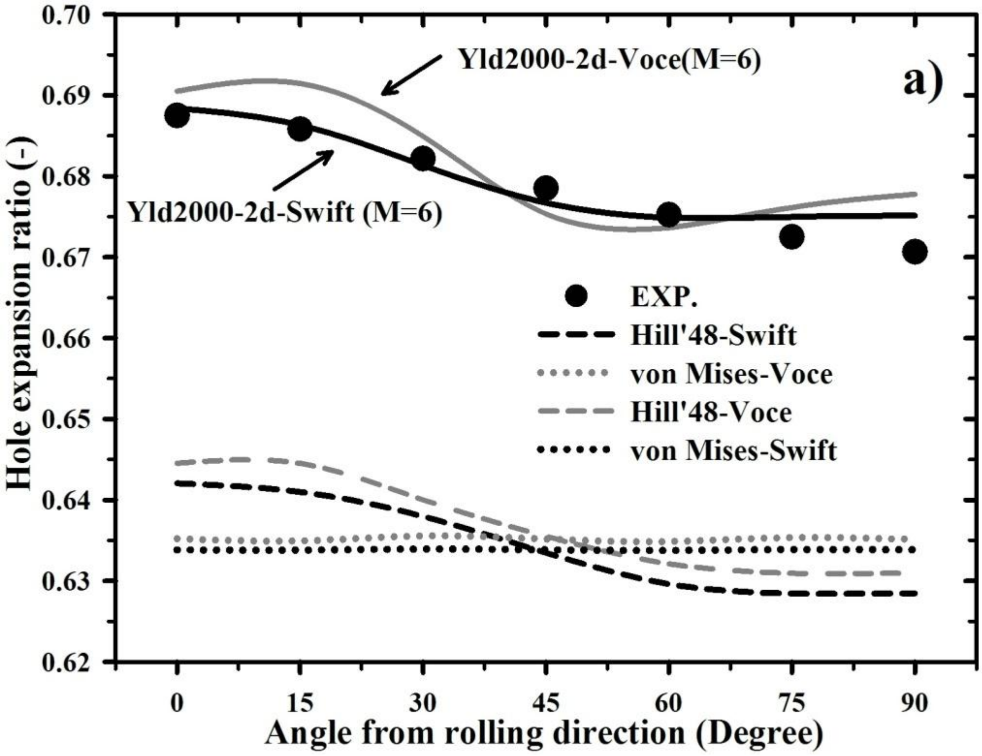

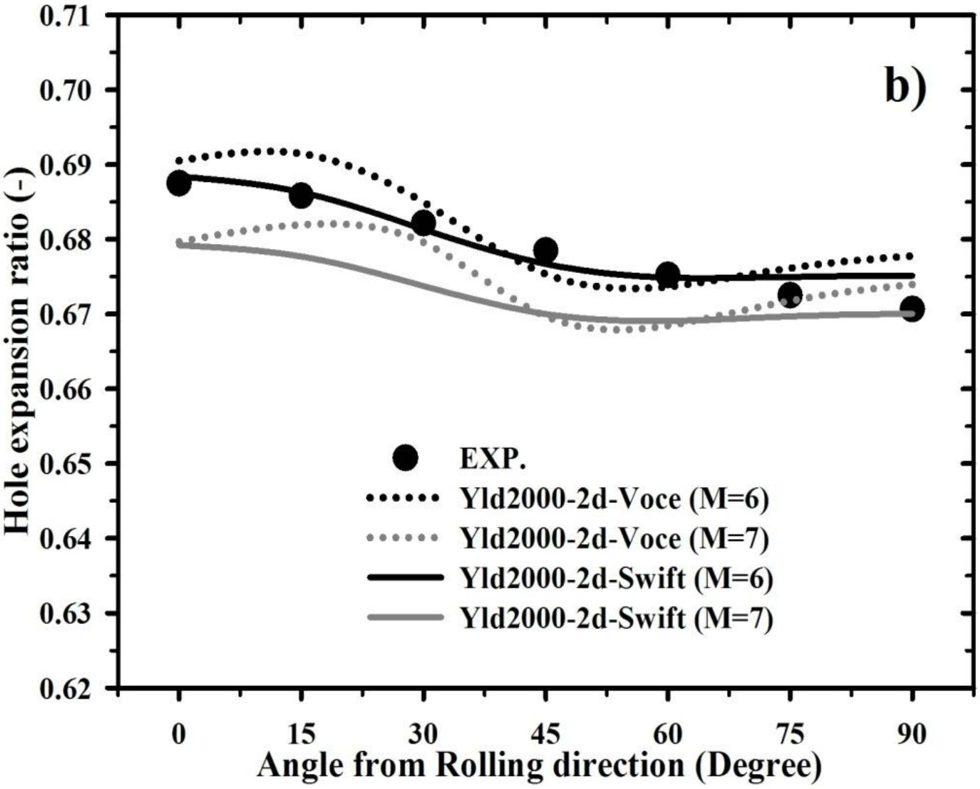

Figure 4.15 Hole expansion ratios along the hole circumference at different angles experimentally determined and calculated by various yield functions coupled with Voce and Swift hardening law and different *M* exponent values in comparison.

4.3.2.3 Influence on thickness strain distribution

Furthermore, Figure 4.16 showed experimentally determined and predicted thickness strain along hole circumference at the moment of failure for different angles. Apparent deviations of the thickness strains from the experiments and simulations were found for all yield criteria, in particular between the angles 0° and 50° from the RD. In contrast, calculated thickness strains along hole circumference between the angles 60° and 90° were more fairly agreed with the experimental values. Essentially, the Yld2000-2d model could at least provide correct tendency of those thickness strains. The von Mises yield model exhibited nearly constant thickness strain along the hole circumference, which thus much differed from the experiments. The resulted thickness strains obtained from the Hill’48 model were also underestimated. Note that deviations in the RD area might be due to uncertainty of the sample geometry measurement after expanding in the experiments, because crack took place at the hole edge in this area. Pre-cracking could occur around the hole edge during preparation process of the samples. This effect was not considered in the simulations that could lead to the differences between experimental and predicted strains. Small effects of the hardening model on the calculated thickness strains were found. The Voce model generally gave lower thickness strains than the Swift model with the exception of the von Mises model. There was no difference between results from the von Mises model combined with both hardening laws. The results obtained by the Swift model were closer to the experiments, as shown in Figure 4.16(a) and Figure 4.16(b). Among all cases, the Yld2000-2d applying the *M* exponent 6 and the Swift law better predicted the thickness strains along the hole circumference. The results from the simulations using the *M* exponent 7 were deteriorated for both hardening laws, as seen in Figure 4.16(b).

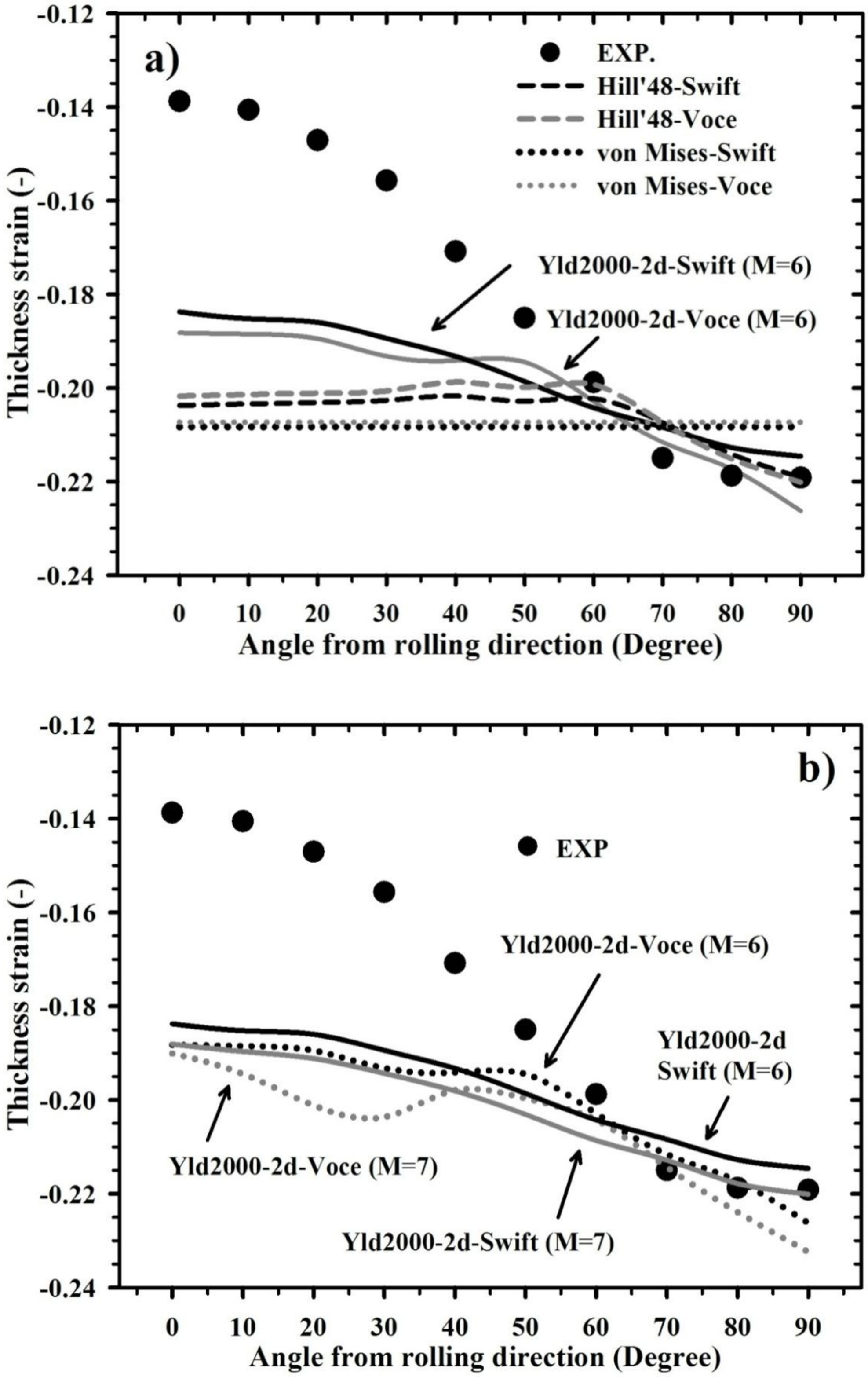

Figure 4.16 Thickness strains along the hole circumference at failure at different angles experimentally determined and calculated by various yield functions coupled with Voce and Swift hardening law and different *M* exponent values in comparison.

The predicted and measured thickness strains distributed along specimen diameter in the RD and TD after failure were illustrated in Figure 4.17 and Figure 4.18. Figure 4.17 demonstrated thickness strains calculated using different yield criteria and hardening models in comparison with experimental data. The FE simulations based on the Yld2000-2d model provided calculated thickness strains along specimen diameter, which were closer to the experiments for both directions. Larger deviations were observed, when the distance from the hole edge became larger. On the TD the thickness strains were nearly constant up to 4 mm from the hole edge. The simulation results, especially those from the Yld2000-2d model, fairly agreed with the experimental strains for both RD and TD directions up to 6 mm from the hole edge. The Hill’48 model exhibited similar tendencies of thickness strain like those from the Yld2000-2d model, but with lower magnitudes, in particular when the distance from the hole edge was larger than 6 mm. The thickness strains predicted by the von Mises model were much underestimated and almost constant for all distances from the hole edge in both directions. There were small influences of the hardening models on predicted thickness strains along specimen diameter in RD and TD as well. The Swift model gave predictions slightly higher than the Voce model in the TD. The results from the von Mises and Hill’48 model coupled with both hardening models were very similar, in which the differences could be neglected. Principally, predictive accuracies of the Hill’48 and von Mises yield criterion were inferior to those of the Yld2000-2d model.

Effects of the hardening models and *M* exponent values were again represented with the Yld2000-2d model in Fig. 21. Both Voce law and *M* exponent 7 showed worse predictions of thickness strain along specimen diameter. The Yld2000-2d criterion coupled with the *M* exponent 7 provided lower thickness strains in all directions for both hardening models than that coupled with the *M* exponent 6. It could be stated that predicted plastic deformations of the investigated TRIP steel were significantly influenced by the yield criterion, hardening model and *M* exponent. In case of hole expansion forming, anisotropic deformation of the steel could be more precisely described by the Yld2000-2d yield model in combination with the Swift law and *M* exponent 6 in all aspects.

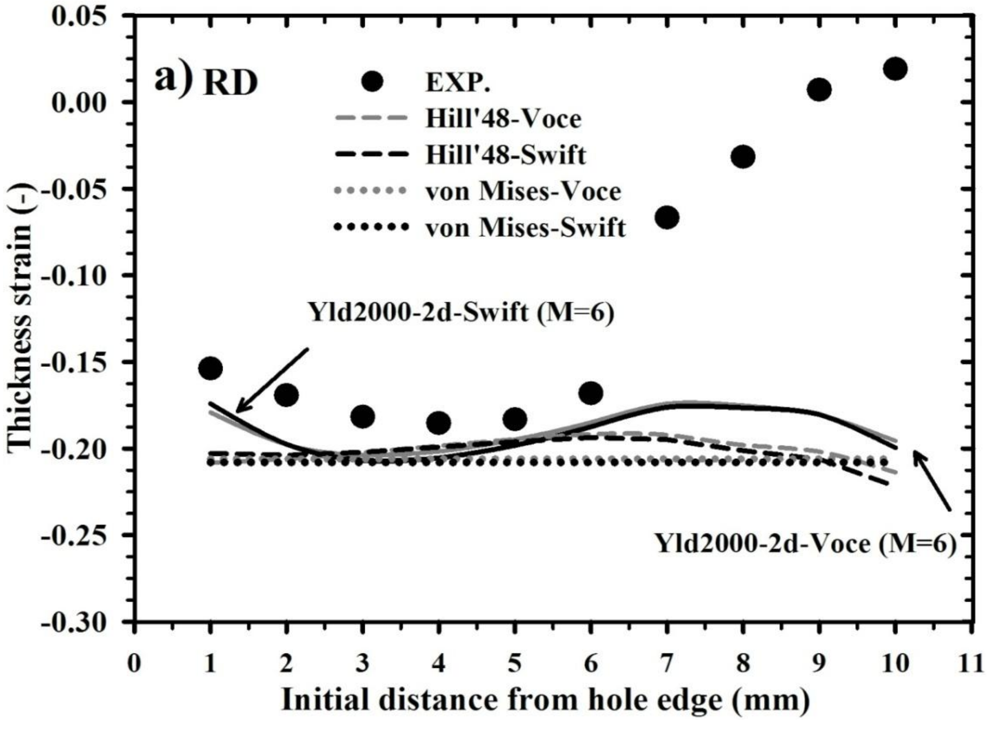

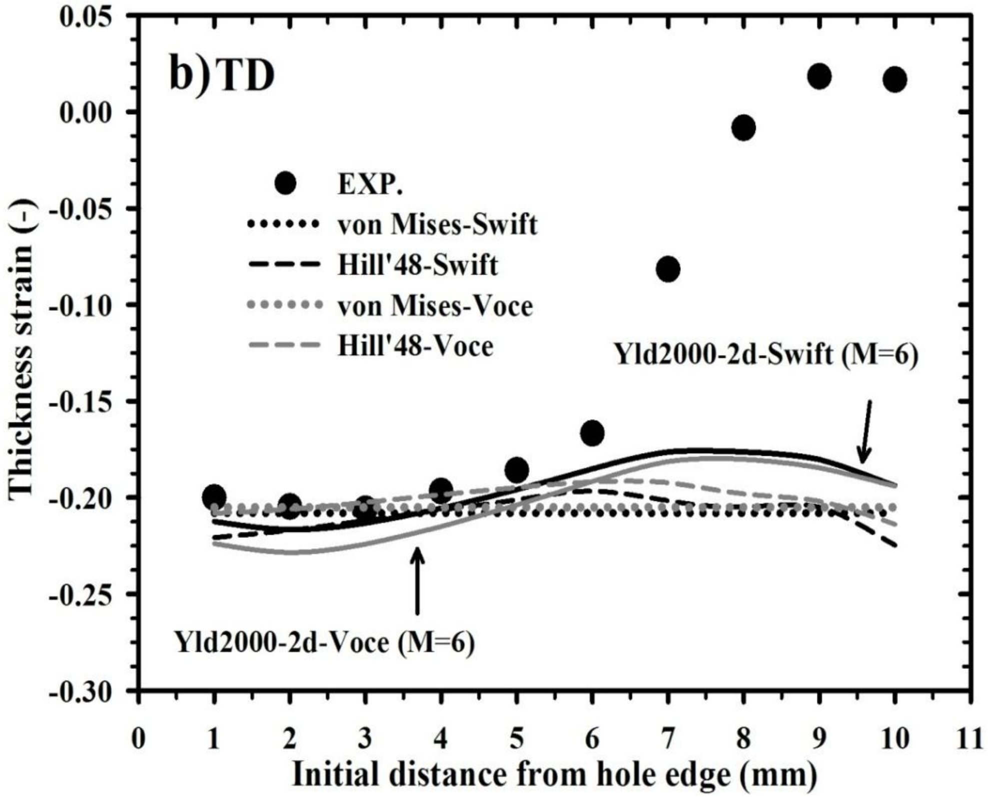

Figure 4.17 Thickness strains along the specimen diameter in the RD and TD at failure experimentally determined and calculated by various yield functions coupled with Voce and Swift hardening law in comparison

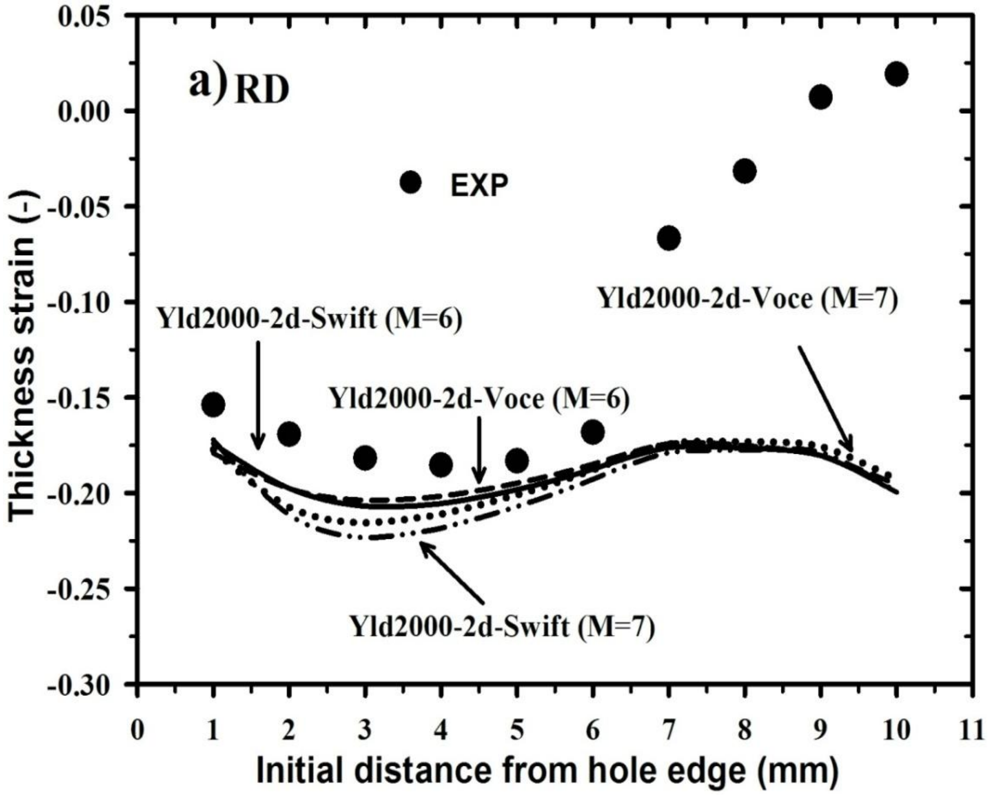

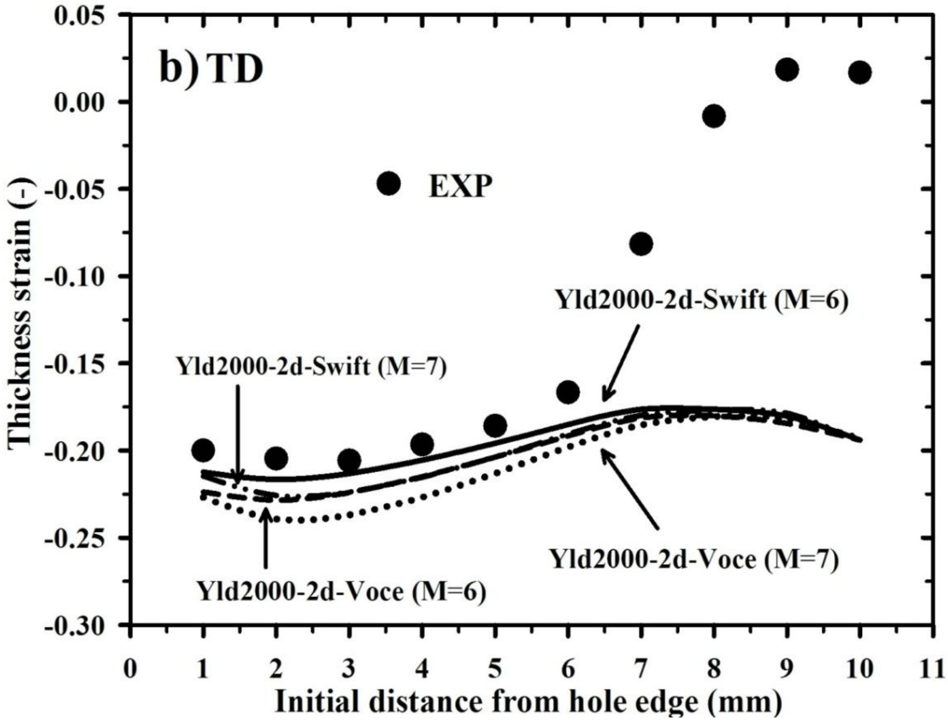

Figure 4.18 Thickness strains along the specimen diameter in the RD and TD at failure experimentally determined and calculated by Yld2000-2d yield criterion coupled with Voce and Swift hardening law and different *M* exponent values in comparison.

4.4 Conclusions

For better understanding of anisotropic plastic behavior of the advanced high strength steel sheet TRIP780, detailed experiments and FE simulations were performed. Uniaxial tension, disk compression and hydraulic bulge test were carried out to investigate material plastic behavior and determine material model parameters. Subsequently, tensile tests of various notched samples and hole expansion tests were experimentally and numerically conducted for verifying different yield and hardening models with regard to local stress–strain distribution during deformation. Three yield criteria, namely, von Mises,Hill'48 and Yld2000-2d model were considered in combination with the Swift and Voce type hardening law. Firstly, normalized flow stresses, yield locus and anisotropy values predicted by different yield criteria were compared, in which those values obtained from the Yld2000-2d model were in good agreement with the experimental results for every condition. Regarding resulting stress–strain curves, FE simulations using the Swift model showed breaking points at much higher plastic strains than those obtained by the Voce model. The Voce model seemed to better describe instant of overall failure of the samples. Early damage initiation occurred before the maximum load could be determined when the predicted stress –strain curves over estimated the experimental results. This damage onset led to subsequent damage evolution and prior softening of the high strength steel during plastic deformation. Influences of the yield criteria and hardening models on developed local stress triaxialities and plastic strains were examined by the tensile samples representing different states of stress. The distributions of stress and strain on the samples were evaluated at the moment of damage initiation. The sample including sharp-edged notch showed stronger effects of yield criterion and hardening law on the local stress distributions than other sample shapes. Obviously, highest stress triaxialities were obtained by theYld2000-2d model in all sample shapes, while the lowest stresses were predicted by the conventional von Mises criterion. In contrast, with the exception of the radius-shape sample, the Yld2000-2d yield model provided lowest local equivalent plastic strains. Different yield functions definitely provided both different local stress and strain values for all considered states of stress. For any types of yield criterion, stress triaxialities obtained from the Swift hardening law were higher than those from the Voce hardening law. Furthermore, the Swift type model obviously exhibited higher plastic strains than the Voce type model, particularly incase of the U-shape sample. A sharper notch shape led to higher stress triaxialities. In principle, maximum stresses occurred in the middle area and maximum equivalent plastic strains resulted at the edges of the samples.

The punch loads and strokes, final hole diameter s interm of hole expansion ratios and strain distributions along the hole circumference and specimen diameter in the rolling and trans-verse directions were investigated with respect to influence of the yield criteria and hardening laws. Principally, the Yld2000-2d model combined with the Swift model and M exponent 6 could more precisely describe all those mentioned values. The Hill'48 model coupled with the Swift model and M exponent 6 provided underestimated results, but with correct tendencies according to the referred direction. The results from the von Misses model, especially the local strains were worse. The hole expansion ratios and thickness strain along the hole circumference were more considerably affected by the applied models than the strain along the specimen diameter.Bette r agreements with the experimental data in any aspect were obtained by the Swift hardening model. The M exponent value significantly affected prediction accuracies of plastic deformation under the holeflanging condition. For the investigated TRIP steel, the M exponent 6 gave fairer prediction than the M exponent7. An appropriate anisotropic yield potential and the hardening law were necessary for representing local plastic deformation behavior of the high strength steel.